Journal of Non-Newtonian Fluid Mechanics 312 (2023) 104978

Contents lists available at ScienceDirect

Journal of Non-Newtonian Fluid Mechanics

journal homepage: www.elsevier.com/locate/jnnfm

3D real time and in situ observation of the fibre orientation during the plane strain flow of concentrated fibre suspensions

T. Laurencin [a,b], Pierre J.J. Dumont [b,*], Laurent Orgéas [a], Steven Le Corre [c], Florian Martoïa [b], Sabine Rolland du Roscoat [a], Patrice Laure [d]

[a] Univ. Grenoble Alpes, CNRS, Grenoble INP, 3SR Lab, F-38000 Grenoble, France
[b] Univ. Lyon, INSA-Lyon, CNRS, LaMCoS, UMR5259, 69621 Villeurbanne, France
[c] Nantes Université, CNRS, Laboratoire de thermique et énergie de Nantes, LTeN, UMR6607, F-44000, Nantes, France
[d] Univ. Côte d'Azur, CNRS, Lab. J.A. Dieudonné, Parc Valrose, F-06000 Nice, France

ARTICLE INFO

Keywords:
Short-fibre composites
Concentrated fibre suspensions
Rheology
X-ray microtomography
3D in situ observations
Fibre kinematics

ABSTRACT

Short-fibre reinforced polymer composites are increasingly used as structural or functional components in many engineering fields. To obtain high-performance composite materials, the polymer matrices are reinforced with high fibre contents (>20–50 wt%). Hence, during their forming, the composites behave as concentrated fibre suspensions that exhibit a non-Newtonian rheology. In addition, their end-use properties depend on the fibre orientation which drastically evolves during the forming operations. Within this context, it is crucial to analyse the induced microstructure changes in flowing concentrated fibre suspensions. For that purpose, 3D in situ compression experiments were performed on model non-Newtonian concentrated fibre suspensions that were imaged using fast X-ray synchrotron microtomography. At the fibre scale, large fluctuations in the translation and rotation of the fibres were observed during compression. These fluctuations were shown to be on the same order of magnitude than the mean fields. They can be attributed to long-range hydrodynamic interactions between neighbouring fibres as well as to short-range interactions induced by the numerous fibre-fibre contacts which practically follow trends predicted by the tube model. Surprisingly, in spite of the chaotic kinematics of the fibres, the macroscopic deformation of the suspension was homogeneous and the flow-induced evolution of fibre orientation was found to be well described by the averaged Jeffery's equation (related to the second order orientation tensor).

1. Introduction

Owing to their interesting mechanical and physical properties, short-fibre reinforced polymer composites are increasingly used as structural and/or functional components in many engineering fields. These composite parts are usually fabricated using cost-efficient forming processes such as injection and compression moulding [1–3]. A wide range of composite materials with tailored physical and mechanical properties can be designed by combining various types of fibrous reinforcements made of synthetic (e.g., carbon, glass, etc.) or natural (e.g., annual plant fibres such as flax and hemp fibres) fibres with varied morphology (shape, aspect ratio) with thermoplastic or thermoset polymer matrices. Short-fibre reinforced polymer composites with high fibre contents (>20–50 wt%) are used as structural parts adapted for high-performance applications (e.g., for the energy and transport industries) [4]. Hence, during their forming, these composites behave as concentrated fibre suspensions with a non-Newtonian rheology [1,5–8]. In addition, their fibrous microstructures undergo large flow-induced restructurations that affect the end-use properties of the produced parts. However, these phenomena are still not well characterised and modelled because of experimental challenges related to the fibre scale observation and analysis of evolving fibrous microstructures and flow mechanisms in non-Newtonian suspending polymer matrices.

Fibres are commonly characterised using several geometric descriptors, namely the fibre aspect ratio $\beta = l/d$ (where l and d are the length and diameter of the fibre, respectively) and its orientation through the unit tangent vector $\mathbf{p}_i = \sin\theta_i\cos\varphi_i\, \boldsymbol{e}_1 + \sin\theta_i\sin\varphi_i\, \boldsymbol{e}_2 + \cos\theta_i \boldsymbol{e}_3$ associated to the fibre main direction, as depicted in Fig. 1:

The study of fibre kinematics was initiated by Jeffery [9] who determined the motion of an ellipsoidal particle immersed in a linear

* Corresponding author.
E-mail address: pierre.dumont@insa-lyon.fr (P.J.J. Dumont).

https://doi.org/10.1016/j.jnnfm.2022.104978
Received 30 September 2022; Received in revised form 16 December 2022; Accepted 20 December 2022
Available online 21 December 2022

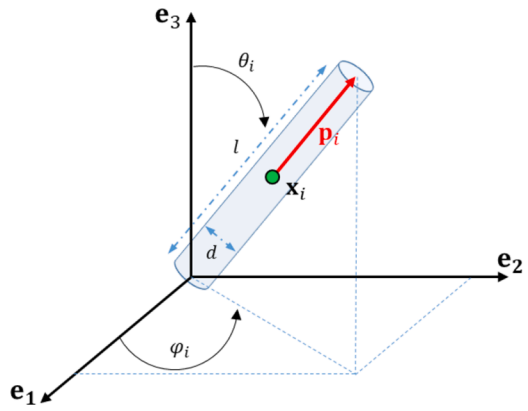

Fig. 1. Coordinate system and definition of fibre descriptors. Note that $\theta_i \in [0,\ \pi]$ and $\varphi_i \in [0,\ 2\pi]$.

and infinite laminar flow field of an incompressible Newtonian fluid. The Jeffery's theory also assumes that the velocity $\mathbf{v}_i$ of the centre of mass of an ellipsoid i is an affine function of the macroscale velocity gradient $\nabla\mathbf{v}$ of the suspending fluid. Hence, for homogenous macroscale fluid flow situations without rigid body motions, the position $\mathbf{x}_i$ of the centre of mass of an ellipsoid i can be predicted by integrating the ellipsoid velocity $\mathbf{v}_i = \nabla\mathbf{v}\cdot\mathbf{x}_i$. In addition, using the first expansion of the fluid velocity field around the particle, the evolution of the ellipsoid orientation can be predicted from the well-known Jeffery's equation, which describes the rate of the unit tangent vector $\mathbf{p}_i$:

$$\dot{\mathbf{p}}_i = \Omega\cdot\mathbf{p}_i + \lambda_b(\mathbf{D}\cdot\mathbf{p}_i - (\mathbf{p}_i\cdot\mathbf{D}\cdot\mathbf{p}_i)\mathbf{p}_i) \tag{1}$$

where $\Omega = (\nabla\mathbf{v} - {}^t\nabla\mathbf{v})/2$ and $\mathbf{D} = (\nabla\mathbf{v} + {}^t\nabla\mathbf{v})/2)$ are the macroscale vorticity and strain rate tensors, respectively, and λ_b is the effective shape factor that can be written as $\lambda_b = 1 - \frac{16.35\ln\beta}{4\pi\beta^2}$ for straight cylindrical fibres with aspect ratio $\beta = l/d$ [10]. The validity of Jeffery's theory was reported by numerous authors [11–14] and extended to any asymmetrical particles by Bretherton [15]. Many rheological models that account for the kinematics of fibres in polymer composites during their forming are based on Jeffery's theory [9]. For these situations, a compact description of the orientation of a collection of fibres is often achieved by computing the fibre orientation distribution function ψ or its moments such as the second $\mathbf{A}$ and fourth order $\mathbb{A}$ orientation tensors, respectively [16].

The predictions of Jeffery's model have been validated [14,17–19] to deal with the fibre kinematics in dilute Newtonian fibre suspensions, where the fibre volume fraction is $\phi \ll 1/\beta^2$ and the average distance between neighbouring fibres is larger than the fibre length l. When the fibre concentration is increased to the semi-dilute regime, defined as $1/\beta^2 \ll \phi \ll 1/\beta$, the fibre kinematics is affected by the presence of neighbouring fibres. In this regime, the average distance between fibres ranges between one fibre length and one fibre diameter. Thus, fibre-fibre interactions can occur, especially long-range hydrodynamic interactions [18,20,21]. In that case, the presence of a fibre within the suspension disturbs the fluid flow, which affects the kinematics of fibres that are in its vicinity. The theoretical estimation of the fibre orientation disturbance induced by long-range hydrodynamic interactions was studied using slender body theory for extensional [18,22] and squeeze flows [21,23]. These studies showed an increase in this disturbance with the increase in fibre concentration. However, this effect was limited by short-range particle screening effects due to multiple interactions that occur with the surrounding fibres (the neighbouring fibres playing a role like a cage) [24,25]. When the fibre concentration is above $\phi > 1/\beta$, the concentrated regime is reached. Short-range interactions induced by fibre-fibre contacts have a predominant effect on the misalignment of fibre trajectories from Jeffery's predictions [7,26–29]. Thus, for the semi-dilute regime, several modifications of Eq. (1) have been proposed in the literature based on the following phenomenological approach of Folgar and Tucker [30,31]:

$$\dot{\mathbf{A}} = (\mathbf{\Omega}\cdot\mathbf{A} - \mathbf{A}\cdot\mathbf{\Omega}) + \lambda_b(\mathbf{D}\cdot\mathbf{A} + \mathbf{A}\cdot\mathbf{D} - 2\mathbb{A} : \mathbf{D}) + 2C_I|\dot{\gamma}|(\boldsymbol{\delta} - \alpha\mathbf{A}) \tag{2}$$

where $\boldsymbol{\delta}$ is the identity tensor, $|\dot{\gamma}| = \sqrt{2\mathbf{D} : \mathbf{D}}$ corresponds to the magnitude of the generalised strain rate, C_I is the (isotropic) orientation diffusivity and with $\alpha = 2$ in two dimensions and 3 in three dimensions. Several expressions of the orientation diffusivity C_I have been proposed, leading to isotropic scalar functions of the fibre concentration and fibre geometry [32,33] or more complex expressions including anisotropic tensorial expressions of the orientation diffusivity [34–36]. Solving Eq. (2) requires the expression of the fourth-order orientation tensor $\mathbb{A}$ which is constructed from a closure approximation from the second-order orientation tensor $\mathbf{A}$ [16,29,37–41].

Jeffery's theory was established to describe the fibre kinematics for flow situations with a good scale separation, meaning that the fibre length should be small compared to the typical dimensions of the flow. However, considering the typical dimensions of the mould gaps, this restrictive condition scarcely occurs during composite forming. Hence, in most situations, the scale separation is low and the flow of short-fibre composites has to be considered as confined [42–44]. Deviations from Jeffery's orbits for fibres in the vicinity of the mould walls or rheometer platens were reported by several authors for particles in suspension in Newtonian fluids [45–47], or non-Newtonian fluids [48–50]. Only few studies described the effects of fibre-mould mechanical interactions on the fibre kinematics by proposing a direct modification of Jeffery's model [51] or using a modified dumbbell approach [52,49].

Considering the complex rheology of polymer composites, several authors also studied the kinematics of single ellipsoidal particles immersed in viscoelastic fluids and subjected to shear flow [53–61]. Deviations from the Jeffery's orbits were observed, showing bistable particle orientations related to the fluid elasticity. However, only a few experimental and theoretical studies accounted for the shear-thinning behaviour of the suspending fluids or elongational flow situations [26,19], although these fluids and flow conditions are commonly encountered in short fibre-reinforced polymer composites. In a previous study [48], the authors showed that during the compression of dilute suspensions with non-Newtonian shear-thinning power-law fluids ($n = 0.2$), the fibre kinematics were not affected by the fluid rheology and were well described by Jeffery's equation (Eq. (1)) for non-confined flows. These experimental results were in accordance with theoretical and numerical models [49].

Owing to the difficulty to observe and characterise in 3D the evolution of the fibrous microstructures during the flow of fibre suspensions, the complex flow mechanisms induced at the fibre scale still remain not well understood. Most of the experimental observations of fibre suspensions were performed using 2D optical techniques [11,12,17,62,63], 2D wide-angle X-ray diffraction [64], high speed X-rays phase-contrast 2D imaging [19] and video camera with isorefractive systems [14,18,21]. These techniques work well for studying dilute suspensions. However, they are inappropriate for the characterisation of semi-dilute and concentrated fibre suspensions. In previous studies [48,49], 3D in situ and real time observations of non-Newtonian shear-thinning dilute and semi-dilute fibre suspensions ($\phi \ll 1/\beta^2$) subjected to lubricated compression experiments were performed using 3D X-ray synchrotron images. Despite the non-Newtonian fluid behaviour and regardless of the investigated experimental conditions (fibre aspect ratio and orientation), Jeffery's theory was also found to be efficient for predicting fibre kinematics when fibres were far enough from compression platens (around 3 times a fibre diameter). Deviations from the affine motion of the fibre centres of mass were also observed experimentally but were not predicted by the simulation. The potential origins of these deviations were attributed to unexpected rigid body motions of the compressed sample or fluid viscoelastic effects.

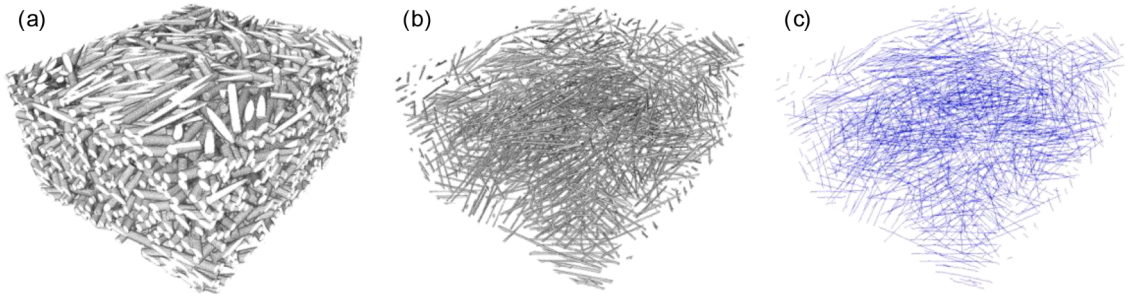

Fig. 2. Illustration of the procedure used to individualise each fibre. (a) Initial 3D image of a concentrated fibre suspension segmented on the fibre phase. (b) Same 3D image obtained after segmentation on the Euclidean distance map calculated on the fibre phase and (c) after skeletonisation and smoothing of fibre centrelines.

Confinement effects were also observed experimentally and numerically on the translation and rotation when fibres entered in contact with the compression platens.

In this context, the objective of this study was to investigate fibre scale flow-induced microstructure changes occurring in concentrated fibre suspensions with non-Newtonian suspending fluid subjected to confined elongational flows. Hence, using a similar procedure to that previously reported in [48,49], model concentrated non-Newtonian fibre suspensions were prepared and compressed using a micro-rheometer that was installed in a synchrotron X-ray microtomograph. 3D in situ and real time observations of the evolving fibrous microstructure were then performed during sample compression. The analysis of the 3D images acquired during these experiments revealed for the first time translation and rotation motions of the fibres during plane strain compression of a concentrated fibre suspension. The kinematics of fibres in concentrated fibre suspensions were compared with the predictions of Jeffery's model.

2. Experimental procedure

2.1. Materials

A hydrocarbon gel was used as suspending fluid [6]. At a temperature of 120 °C the gel behaved as a Newtonian fluid and its shear viscosity was approximately 1 Pa s. At room temperature, the gel was solid which enabled the fibrous microstructure to be "frozen" and facilitated the handling of the suspension. At a temperature of 50 °C, the gel exhibited a non-Newtonian behaviour close to that of industrial polymer matrices used in composites. The gel viscosity in shear could be modelled as a shear-thinning fluid of power law type, i.e., $\eta_m = K|\dot{\gamma}|^{n-1}$ with a consistency $K = 440$ Pa.s^n and a power-law index $n = 0.2$. The parameters K and n were determined using classical rheometry experiments (Anton Paar MCR301 rheometer equipped with a cone-plane geometry).

Short fibres used in the model suspensions were obtained from continuous elastic fishing wire (diameter $d = 200$ μm, length $l = 1500$ μm, i.e., $\beta = 7.5$, Young's modulus $E = 2$ GPa). Model concentrated fibre suspensions with 3D random fibre orientation were prepared manually using an experimental procedure that slightly differed from that already reported by Laurencin et al. [48]. Briefly, this procedure consisted in projecting fibres inside the cavity of a mould. This allowed obtaining a fibre mat with a fibre orientation comprised between a 2D in-plane random fibre orientation and a 3D one. Then this fibre mat was impregnated by the hydrocarbon gel heated at 120 °C and subjected to vibration to remove the air bubbles that could possibly be entrapped. Finally the as-obtained suspensions were cooled down to ambient temperature. To determine the fibre volume fraction ϕ (and thus the total number of fibres N) required to obtained fibre suspensions in the concentrated regime, i.e., suspensions with a mean coordination number z (mean number of fibre-fibre contacts per fibre), greater than 1, we used the statistical tube model [65] the estimates of which for these types of fibrous media were shown to be relevant [6,66]:

$$z = 4\phi\left(\frac{2}{\pi}\beta\Phi_1 + \Phi_2 + 1\right) \tag{3}$$

where the orientation functions Φ_1 and Φ_2 can be estimated from the knowledge of the tangent unit vectors $\mathbf{p}_i$ and the total number N of fibres as follows:

$$\Phi_1 = \frac{1}{N^2}\sum_{i=1}^{N}\sum_{j=1}^{N}\|\mathbf{p}_i \times \mathbf{p}_j\| \quad \text{and} \quad \Phi_2 = \frac{1}{N^2}\sum_{i=1}^{N}\sum_{j=1}^{N}\left|\mathbf{p}_i \cdot \mathbf{p}_j\right| \tag{4}$$

Note that $\Phi_1 = \pi/4$ and $\Phi_2 = 1/2$ for fibrous structures with a 3D random fibre orientation [65].

Following this procedure, several cuboids (in-plane dimensions $w_0 \times w_0 = 8 \times 8$ mm^2 and height $h_0 = 2.2$ mm) with $\phi = 40\%$ (or conversely $N = 2770$) were obtained.

2.2. Plane strain compression experiments with real-time 3D in situ X-ray imaging

Samples were subjected to lubricated plane strain compression loading at a temperature of 50 °C using a specific micro-rheometer [48,49,67]. The micro-rheometer was mounted on the rotation stage of a synchrotron X-ray microtomograph (TOMCAT beamline, Swiss Light Source, Paul Scherrer Institute, Villigen, Switzerland) which enabled 3D in situ images of the evolving fibrous microstructure to be acquired in real-time conditions. To maintain the fibre suspension at a constant temperature of 50 °C, heaters and thermocouples were inserted inside the compression platens. Before compression, the platens were lubricated with silicone oil (47 V1000–80,026, Chimie-Plus Laboratoires), and the suspensions were subjected to a small pre-compression to ensure a good mechanical contact. After a stress relaxation and temperature homogenisation (~10 min) the mechanical loading was applied continuously through a piezoelectric actuator attached to the lower compression platen. Plane strain compression experiments were performed at a constant velocity $\dot{h} = 11$ μm s^{-1} of the lower platen, corresponding to an initial strain rate $D_{33} = \dot{h}/h_0 = 0.005$ s^{-1} along the $\mathbf{e}_3$-direction. A load cell of 5 N was also placed under the upper compression platen and used to measure precisely the axial force F exerted on the sample in the $\mathbf{e}_3$-direction. Then, by assuming the suspension incompressibility, the axial compression stress $\sigma_{33} = |F|h/(h_0 w_0^2)$ was plotted as a function of the axial compression Hencky strain $|\varepsilon_{33}| = |\ln(h/h_0)|$ (up to 0.5). Note that the suspension flow was considered to be confined because of the poor scale separation, i.e., $l/h = \mathcal{O}(1)$. To acquire 3D X-ray microtomography images of the suspension during compression, the X-ray energy and the number of radiographs (dimensions of the images: 1776 × 1776 pixels) were set to 20 keV and 600, respectively. The scan duration was 0.42 s. 3D images of the scanned specimen with a size of 1776 × 1776 × 450 voxels for a voxel size of 11 × 11 × 11 μm^3 were obtained using the phase-contrast Paganin reconstruction mode [68,69] and suitable reconstruction

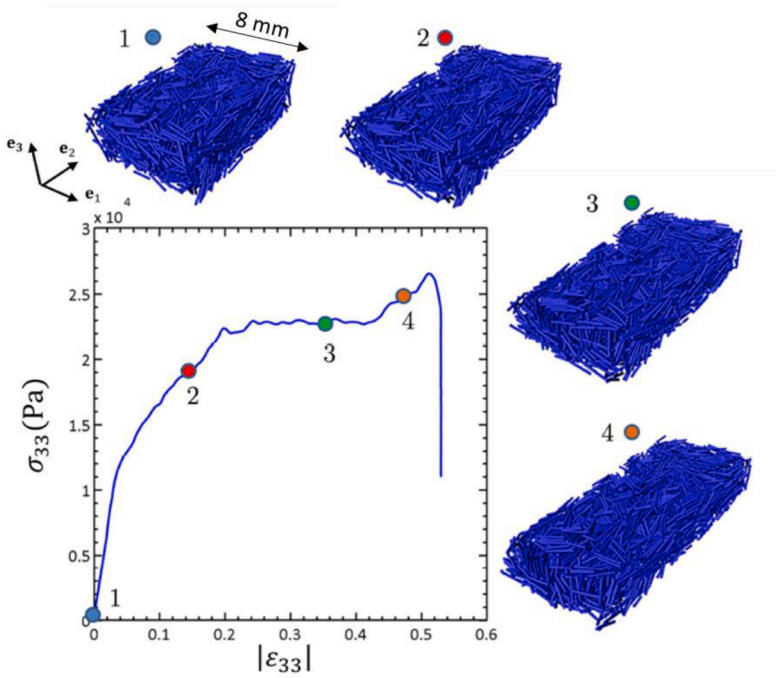

Fig. 3. Plane strain compression of a model concentrated suspension containing 2770 fibres ($\phi = 40\%$). The graph shows the evolution of the compression stress σ_{33} measured along the $\boldsymbol{e}_3$ axis as a function of the compression strain $|\varepsilon_{33}|$. 3D images numbered from 1 to 4 show the evolution of the fibre microstructure during lubricated plane strain compression. Numbers on the curves show the corresponding stress and strain states to these images.

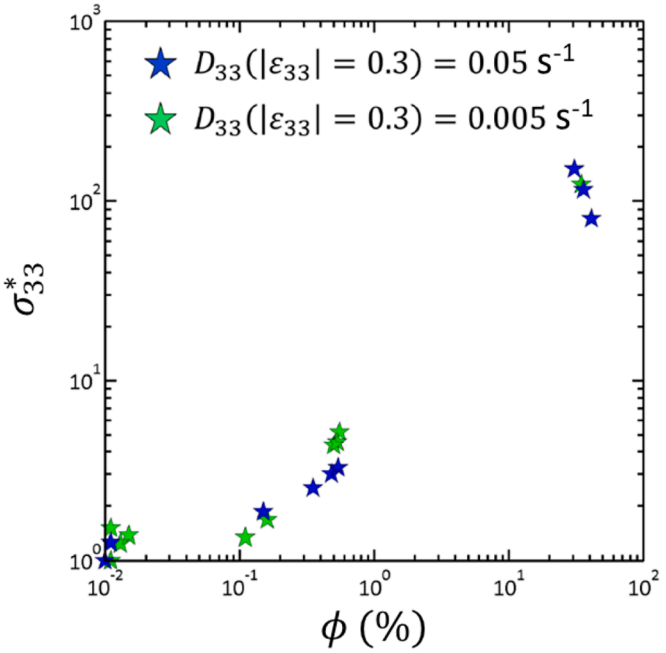

Fig. 4. Evolution with the fibre content ϕ of the dimensionless compression stress σ^*_{33} for various model fibre suspensions ($\beta = 7.5$) that were prepared following the procedure described in Section 2.1.

algorithms.

2.3. Image analysis and data post-treatment

To detect and quantitatively follow the evolution of the fibrous microstructure during lubricated plane strain compression, several image analysis operations were performed following the methodology reported by Latil et al. [67]. After a segmentation step of images on the fibrous phase (Fig. 2a), the numerous contacts between fibres did not enable each fibre to be clearly distinguished. To individualise the fibres, a 3D distance analysis between the two phases (i.e., fibre and fluid) was applied (Fig. 2b). This stage consisted in calculating the distance of each voxel of the fibrous phase with the fluid phase and attributing a new grey level value to the considered voxel. Then, the as-obtained 3D Euclidian distance map was segmented. This operation enabled the removal of all the fibre-fibre contacts by reducing the fibre diameter. The fibre centrelines were extracted using a skeletonisation algorithm [70], namely the distance ordered homotopic thinning algorithm implemented in Avizo software (Fig. 2c).

The centreline of each fibre i was smoothed and fitted using a linear parametric curve with coordinate $\mathbf{x}_i(s)$ along the curvilinear abscissa s of the considered fibre i. Then, a local Frenet basis was associated to each coordinate $\mathbf{x}_i(s)$, using the procedure reported in [67,71]. In this local basis, $\mathbf{t}_i$ is the unit tangent vector, $\mathbf{n}_i$ and $\mathbf{b}_i$ are the unit normal and binormal vectors, respectively. Hence, the set $(\mathbf{x}_i, \mathbf{t}_i, \mathbf{n}_i, \mathbf{b}_i)$ enabled the description of the local geometry of the fibres, their orientation ($\mathbf{p}_i$ corresponds to the average of all unit vectors $\mathbf{t}_i$ along the curvilinear abscissa s of the fibre i), and the orientation and position of each fibre-fibre contact.

The set C of fibre-fibre contacts was extracted from the 3D images using the procedure reported in [66,67]. This procedure was based on the calculations of the distances between the fibre centrelines. A fibre–fibre contact was detected when the local distance between two neighbouring fibre centrelines was less than or equal to a fibre diameter d. Hence, it was possible to estimate the mean coordination numbers z in the studied suspensions for each compression stage. In addition, the unit normal vector $\mathbf{c}_\alpha$ of each contact α ($1 \leq \alpha \leq C$) between two contacting fibres i and j was calculated as follows: $\mathbf{c}_\alpha = \mathbf{p}_i \times \mathbf{p}_j$.

Doing so, it was also possible to analyse the overall orientation of fibres and fibre-fibre contacts by using deterministic estimates of the second $\mathbf{A}$ and the fourth $\mathbb{A}$ order fibre orientation tensors [6,67]:

$$\mathbf{A} = \frac{1}{N}\sum_{i=1}^{N} \mathbf{p}_i \otimes \mathbf{p}_i \ \textbf{and}\ \mathbb{A} = \frac{1}{N}\sum_{i=1}^{N} \mathbf{p}_i \otimes \mathbf{p}_i \otimes \mathbf{p}_i \otimes \mathbf{p}_i \quad (5)$$

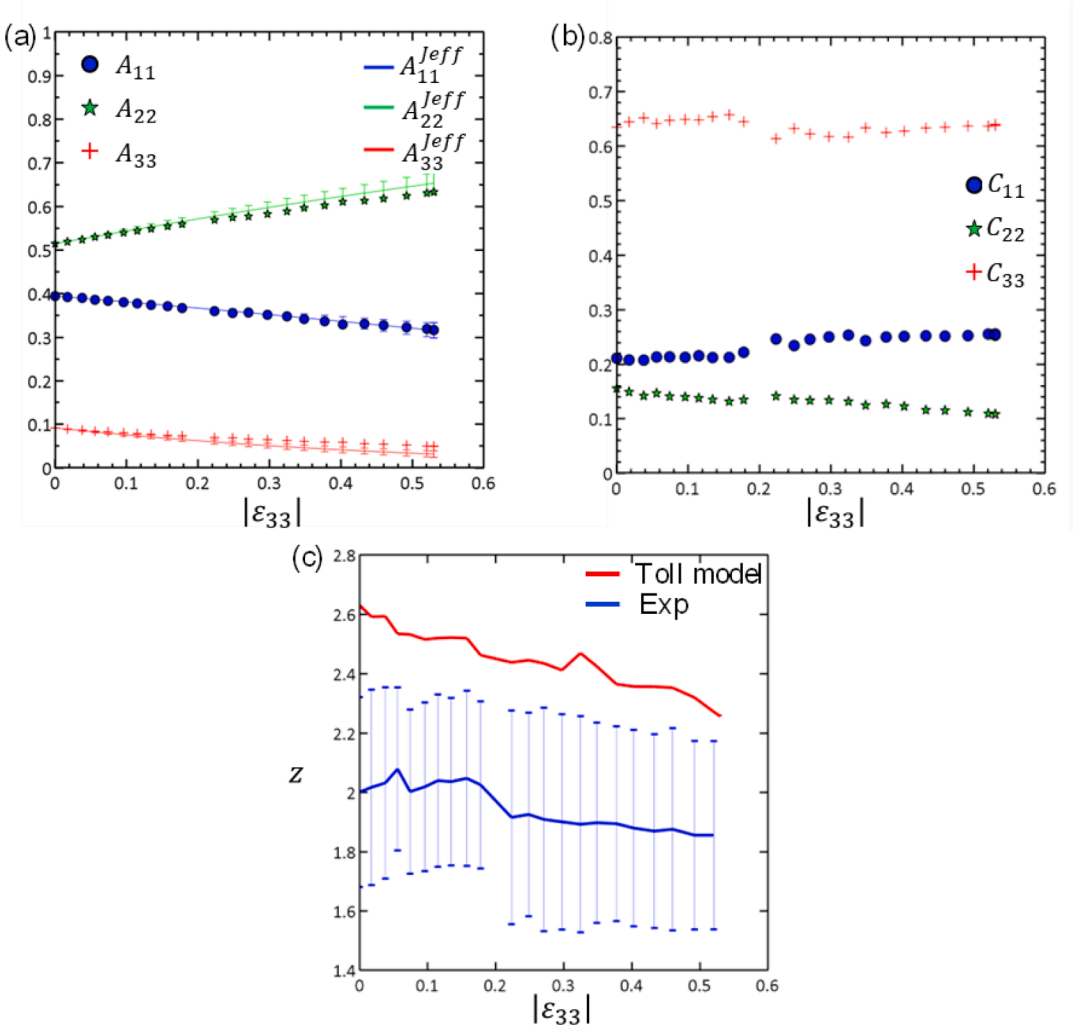

Fig. 5. (a) Evolution of the diagonal components A_{ii} of the measured second-order fibre orientation tensor **A** with the sample compression strain $|\varepsilon_{33}|$. The continuous lines represent the predictions of the calculated second order orientation tensor A_{ii}^{Jeff}. (b) Evolution of the diagonal components C_{ii} of the second order orientation contact tensor **C** with the sample compression strain $|\varepsilon_{33}|$. (c) Evolution of the mean coordination number z with the sample compression strain $|\varepsilon_{33}|$. The blue and red curves represent the mean coordination number z that was directly measured from the 3D images shown in Fig. 3 and that predicted by the statistical tube model (Eq. (3)), respectively.

and the second order orientation contact tensor **C** [6,7,29,67,72,73]:

$$\mathbf{C} = \frac{1}{C}\sum_{\alpha=1}^{C} \mathbf{c}_\alpha \otimes \mathbf{c}_\alpha \tag{6}$$

In addition, fibre positions, orientations and fibre-fibre contacts were tracked between each compression step. The rigid motion of fibres was followed using a fibre centreline tracking algorithm based on a correlation distance function [74]. Briefly, the principle of the correlation method consists in recognizing the fibre i from a so-called initial configuration of the fibre suspension at time t among the N fibres j of a so-called deformed configuration of the suspension at time $t + dt$. This method relies on the minimisation of the following discrete correlation function M_{ij} defined as follows:

$$M_{ij} = \sum_{i}^{N}\sum_{j}^{N}\sum_{k} \| \mathbf{x}_i^t(s_k) - \mathbf{x}_j^{t+dt}(s_k) \| \tag{7}$$

For each couple (i,j), the function M_{ij} represents the inter-fibre distance calculated from the spatial coordinates $\mathbf{x}_i^t(s_k)$ and $\mathbf{x}_j^{t+dt}(s_k)$ along the curvilinear abscissa s_k of the fibre centrelines. Minimising this function M_{ij} enables finding for each fibre i its corresponding fibre j. The validity of each fibre association is checked by using again the correlation technique to recognize each fibre j at time $t + dt$ among the N fibres i at time t. The correlation is validated if the couples (i,j) of associated fibres obtained from both minimisation processes are identical.

The relevance of Jeffery's model was assessed by testing the validity of the affine assumption (i.e., $\mathbf{v}_i^{Jeff} = \nabla\mathbf{v}\cdot\mathbf{x}_i^{Jeff}$), and the orientation equation (Eq. (1)) for the predictions of the position of the centre of mass $\mathbf{x}_i^{Jeff}$ and the orientation vector $\mathbf{p}_i^{Jeff}$ of each fibre i of the model suspensions. These equations were numerically solved using a fourth order Runge-Kutta integration scheme implemented in Matlab. Previous measurements made on dilute fibre suspensions [48] revealed that the macroscale suspension flow was homogeneous, incompressible ($\nabla\cdot\mathbf{v} = 0$) and irrotational ($\mathbf{\Omega} = \mathbf{0}$). Therefore, the strain rate tensor **D** was estimated from the height of the suspension h measured using the 3D images with an error of ± 1 voxel. The initial positions $\mathbf{x}_i^0$ and the initial orientation vectors $\mathbf{p}_i^0$ were taken from the initial undeformed configuration of the suspension measured on the 3D images, with maximum errors of ± 1 voxel and $\pm 0.15°$, respectively. Then, two thousand integrations per experiment were computed using errors associated with h, $\mathbf{x}_i^0$ and $\mathbf{p}_i^0$ that were randomly chosen within the aforementioned ranges. Hence, the errors on the corresponding integrated parameters could be

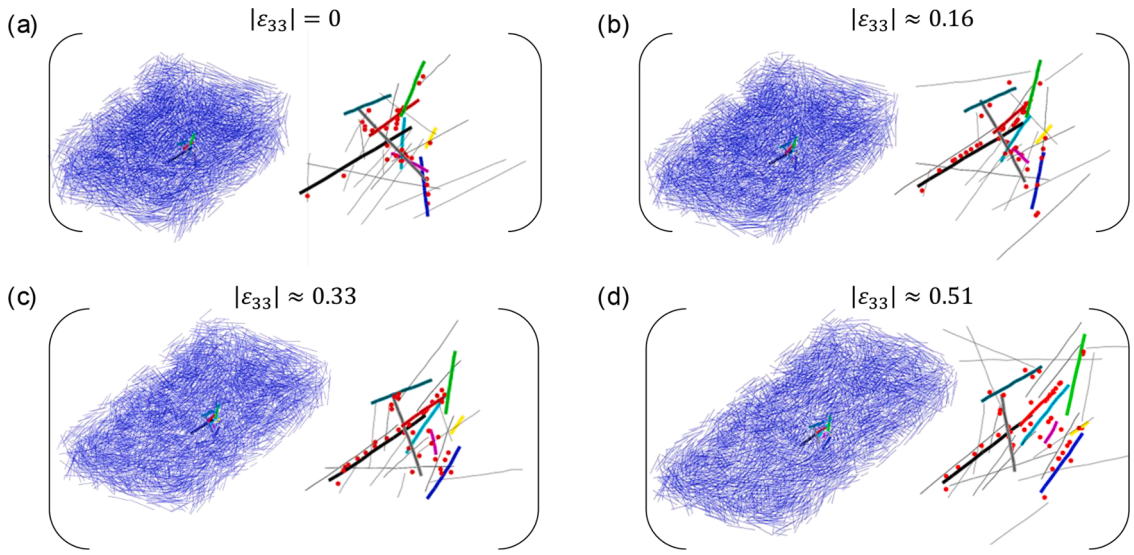

Fig. 6. (a–d) Left-hand side 3D images: identified fibre centrelines during the plane strain compression of a concentrated fibre suspension at various compression strains $|\varepsilon_{33}|$. (a–d) Right-hand side images: zoomed views in the core of the sample. These zoomed images show the evolution of the kinematics (positions and orientations) of nine fibres (represented by thick coloured lines) that were selected in the centre of the sample. The evolution of their discrete contacts with their neighbouring fibres (represented by thin grey lines) is also shown and represented by red dots.

estimated. The errors were considered to correspond to the difference between the 2nd and 98th percentile values of the computed distributions. Finally, the calculated orientation vectors $\mathbf{p}_i^{Jeff}$ from the integration of Eq. (1) enabled the second order fibre orientation tensor $\mathbf{A}^{Jeff}$ to be directly calculated again from Eq. (5). The as-calculated tensor $\mathbf{A}^{Jeff}$ could be compared to the tensor $\mathbf{A}$ measured from the 3D images.

3. Results and discussion

3.1. Flow mechanisms at the sample scale

Fig. 3 shows the typical evolution of the stress σ_{33} measured along the e_3 axis during the plane strain compression of a model concentrated fibre suspension. 3D views of the fibrous structure obtained at various strain $|\varepsilon_{33}|$ are also shown in this figure. The compression curves of concentrated fibre suspensions exhibit two regimes: a first regime where the stress increases non-linearly up to a flow stress $\sigma_{33} \approx 2.3 \times 10^4$ Pa followed by a plateau-like regime. Note that in these flow conditions, the contribution of the suspending fluid scales as 295 Pa which demonstrates the crucial of fibres on the rheology of the studied suspensions. In the same time, the 3D images reveal that the fibre microstructure is compressed along the $\boldsymbol{e}_3$ axis but also flows along the channel's axis in the $\boldsymbol{e}_2$ direction. At the macroscale, the flow of the suspension is homogeneous and corresponds to an incompressible plug-like flow without any phase separation between the fibres and the polymer matrix. This tends to show that despite the high concentration of the suspension, the entanglement of the fibrous network is sufficiently low to enable the fibres to move relatively to each other under the applied compression stress.

Fig. 4 shows the evolution with ϕ of the dimensionless compression stress $\sigma_{33}^* = \sigma_{33}(\phi)/\sigma_{33}(\phi = 0)$, where $\sigma_{33}(\phi)$ and $\sigma_{33}(\phi = 0)$ are the axial compression stresses of the fibre suspension and the polymer matrix, respectively, that were measured at a compression strain $|\varepsilon_{33}| = 0.3$. For comparison purpose, we have also plotted the dimensionless compression stresses σ_{33}^* obtained for various model fibre suspensions in the dilute and semi-dilute regimes prepared in the same conditions and with the same fibre aspect ratio $\beta = 7.5$ [48,49]. This shows that the compression stress required for the flow establishment of a concentrated fibre suspension (i.e., suspensions with $\phi = 0.4$) is ten times higher than that measured for semi-dilute fibre suspensions. In addition, this figure emphasises the weak (resp. pronounced) effect of the compression strain rate D_{33} (resp. ϕ) on the dimensionless compression stress σ_{33}^*.

The graphs in Figs. 5a,b show the evolution of the diagonal components of $\mathbf{A}$ and $\mathbf{C}$ tensors. Note that it was checked that the diagonal components could reasonably be associated to the principal components of these two tensors. These graphs reveal that the fibre orientation of the initial suspension exhibited a 3D transverse isotropy (*i.e.*, $A_{11} \sim A_{22} \neq A_{33}$) with a high density of unit normal vectors $\mathbf{c}_\alpha$ of fibre-fibre contacts orientated along the $\boldsymbol{e}_3$ axis (i.e., $C_{33} > C_{11} \approx C_{22}$). These features were presumably inherited from the sample preparation since each fibre of the suspension was introduced into the suspending fluid from the top, along the $\boldsymbol{e}_3$ axis. The evolution of the diagonal components of $\mathbf{A}$ and $\mathbf{C}$ tensors with the compression strain $|\varepsilon_{33}|$ revealed that the fibres tended to reorient along the channel's axis $\boldsymbol{e}_2$. This is illustrated by the increase of the components A_{22} and C_{11} with the increase in the compression strain $|\varepsilon_{33}|$. Then, it is interesting to notice that C_{33} did not evolve, proving that the density of unit normal vectors of fibre-fibre contacts remains almost the same.

Fig. 5c shows the evolution of the mean coordination number z as a function of the sample compression strain $|\varepsilon_{33}|$. The error bars shown in the graph correspond to an error of ± 1 voxel that was related to the extraction procedure of the centerlines of each fibre of the suspension. This figure shows that the mean coordination number z was initially close to 2. This proves that the studied suspension was in the concentrated regime and that the fibres formed a connected network. In addition, this graph shows that z slightly decreased with increasing the compression strain $|\varepsilon_{33}|$. This evolution could be related to the flow-induced orientation of fibres along the $\boldsymbol{e}_1$ axis. It is well-established [65,75,76] that the mean number of fibre-fibre contacts decreases as the fibres orientate along a preferred/principal direction. It is important to notice that this trend is also well reproduced by the statistical tube model [65] even if the theoretical predictions of z are slighly higher than the measurements. This results is in agreement with several observations made from 3D images of fibrous materials by Orgéas et al. [66] and Guiraud et al. [6].

3.2. Flow mechanisms at the fibre and fibre-fibre scale

Using the correlation technique [74], it was also possible to analyse the flow mechanisms and the complex microstructure of fibre

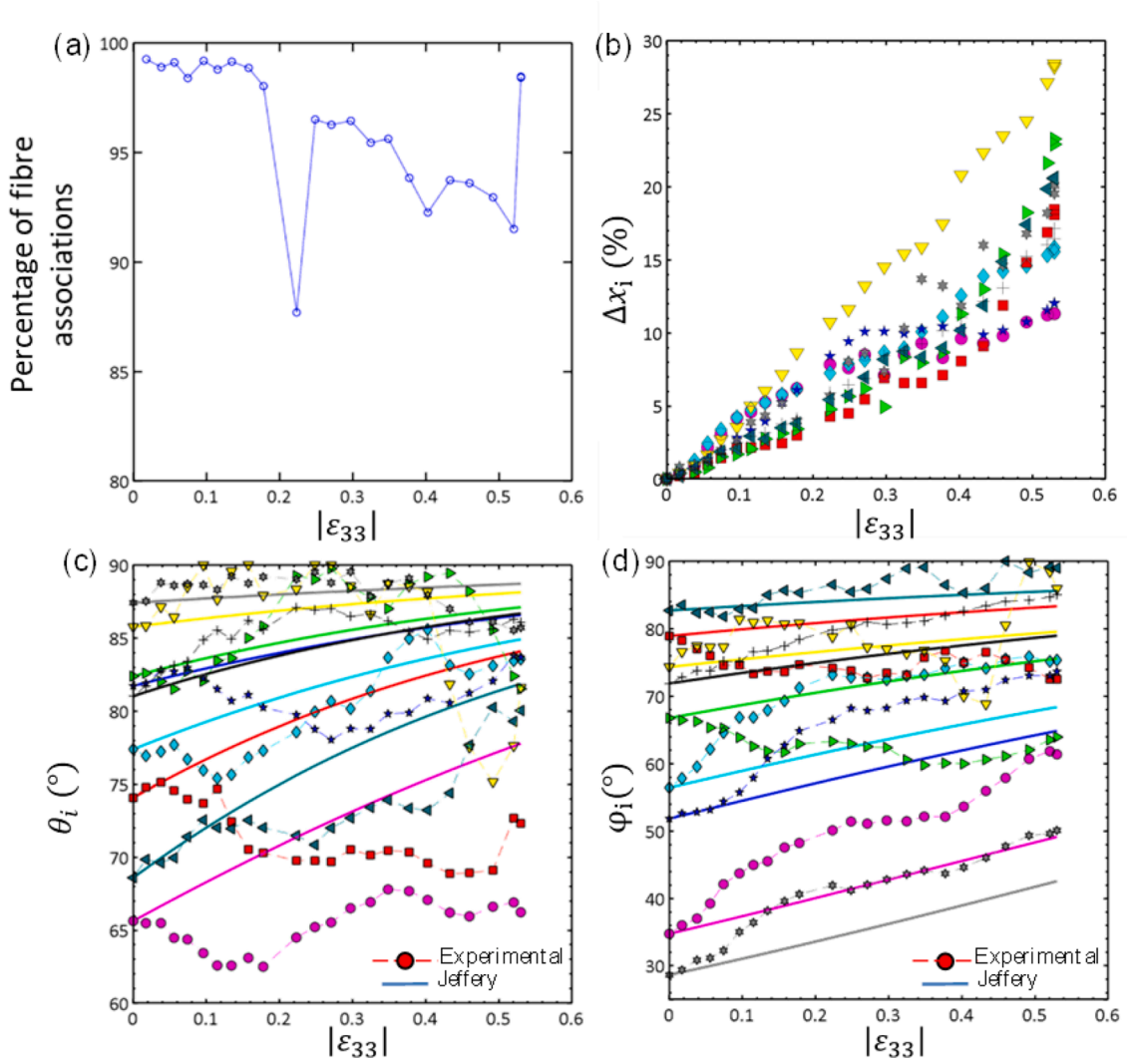

Fig. 7. (a) Graph showing the percentage of fibre associations obtained using the semi-discrete correlation method of the fibre centrelines as a function of the sample deformation $|\varepsilon_{33}|$. (b–d) Graphs showing the evolution of the deviations Δx_i (b), angles θ_i (c) and φ_i (d) of nine tracked fibres taken in the centre of the sample as a function of the compression strain $|\varepsilon_{33}|$.

suspensions under flow at the fibre and contact scale. In particular, it was possible to describe the kinematics of single fibres that could be recognised, identified and followed during plane strain compression (Fig. 6).

The graph in Fig. 7a shows the performance of the used semi-discrete correlation procedure. This graph shows the evolution during a plane compression experiment of the percentage of good fibre associations obtained by correlation between discretised 3D images at a compression deformation state $|\varepsilon_{33}|$ and that at $|\varepsilon_{33}| + \Delta|\varepsilon_{33}|$. Thanks to the recent progress offered by synchrotron radiation facilities, 3D high resolution images were obtained at a sufficiently high frequency, i.e., with deformation increments between images $\Delta|\varepsilon_{33}| < 0.03$, thus leading to a high percentage (>90%) of fibre associations. Hence, as shown in Fig. 6, it was possible to track the positions and orientations of a selection of neighbouring fibres taken at the centre of the sample as well as the positions and the number of contacts between them. The 3D images on the left-hand side show all fibre centrelines and their evolution for various deformation state $|\varepsilon_{33}|$ of the sample subjected to plane strain compression. The images on the right-hand side are zoomed views in the core of the sample where the fibre centrelines of tracked fibres appear in the form of coloured thick lines and their discrete contacts with the neighbouring fibres (represented by thin grey lines) are symbolised by red dots (Fig. 6).

The graph in Fig. 7b shows the evolution with $|\varepsilon_{33}|$ of the deviation $\Delta x_i = \| \mathbf{x}_i - \mathbf{x}_i^{Jeff} \|$ of the experimental position of the fibre centres of mass $\mathbf{x}_i$ with respect to $\mathbf{x}_i^{Jeff}$ of the nine tracked fibres. In addition, the two graphs c-d in Fig. 7 show the evolution of the orientation angles θ_i and φ_i of the nine tracked fibres as a function of the macroscopic compression strain $|\varepsilon_{33}|$. For comparison purpose, the evolution of the orientation angles predicted by Jeffery's model (continuous lines) are also plotted in this figure. These three graphs clearly illustrate the erratic motion of these fibres in their network. The graph b reveals that the translation motion of tracked fibres was different from that they should follow under the affine field assumption. These deviations are much more pronounced than those observed for dilute and semi-dilute fibre suspensions [48,49]. As discussed in these previous studies, it is difficult to determine whether the general trend of the deviations had physical origins (e.g. small shear flow related to non-ideal lubrication conditions between the samples and the compression platens) or were induced by experimental artefacts (e.g. unexpected rigid body motions of samples). However, the evolution of Δx_i of the analysed fibres also revealed that they were subjected to several events (related for instance to the loss or creation of fibre-fibre contacts) that induced pronounced and erratic variations in the position of their centres of mass. Some of these events are clearly visible for the blue fibres in the graph b of Fig. 7 (see the large

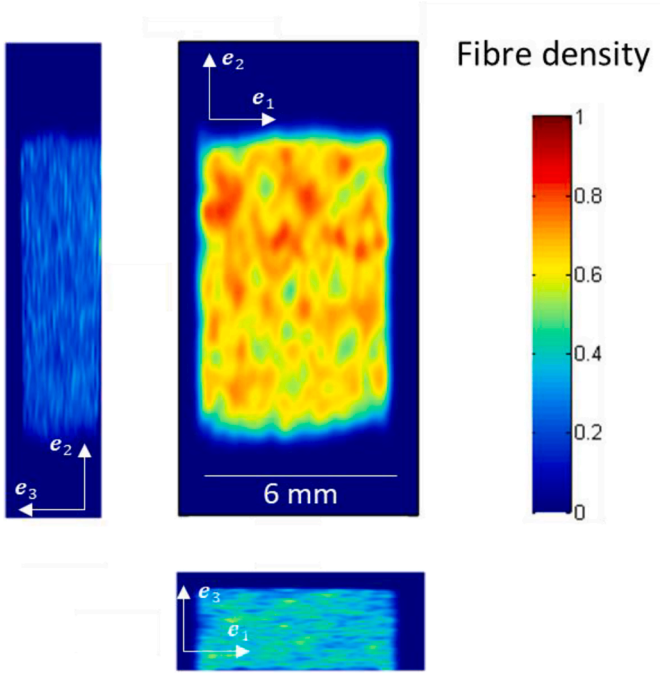

Fig. 8. 2D map showing the fibre density in the suspension (for a compression strain of $|\varepsilon_{33}| = 0.2$) obtained thanks to the "Bivariate Kernel Density Estimator" function implemented in Matlab from the fibre centrelines projected in the $(\boldsymbol{e}_2, \boldsymbol{e}_3)$, $(\boldsymbol{e}_1, \boldsymbol{e}_2)$ and $(\boldsymbol{e}_1, \boldsymbol{e}_3)$ planes, respectively. These maps show the presence of fibre mesostructures or aggregates within the fibre suspension, in particular in the $(\boldsymbol{e}_1, \boldsymbol{e}_2)$ plane.

variations in the positions of the blue points). Note also that all the analysed fibres from graph b were affected by this type of events.

In addition, the graphs of Figs. 7c-d reveal that the rotation of each fibre was extremely erratic and showed large fluctuations, i.e., a behaviour far from that predicted by Jeffery's equation (depicted by the continuous lines), as revealed by the fluctuations of the θ_i and φ_i angles measured during compression. The rotation of these fibres was presumably hindered by their contacts with their neighbouring fibres (zoomed views of Fig. 6). For the highest compression strain, almost all the fibres tended to align along the main flow direction (increase of θ_i and φ_i angles). However, some fibres exhibited an inverse trend, see for instance the yellow, green and red fibres.

These results obtained in the core of the sample, i.e., in a zone far from the two platens, are different from those observed for dilute and semi-dilute fibre suspensions [48,49]. In the present case, the erratic translation and rotation motions of fibres were induced by the multiple interactions between fibres. However, in spite of the chaotic kinematics of individual fibres it is interesting and surprising to notice that the macroscopic deformation of the sample remained homogeneous and the overall fibre orientation of the suspension could be well predicted by the second order fibre orientation tensor $\mathbf{A}^{Jeff}$ (Fig. 5a).

4. Conclusion

The objective of this study was to observe and characterise at the fibre scale, the flow mechanisms occurring in concentrated fibre suspensions. For that purpose, model concentrated fibre suspensions with a non-Newtonian suspending fluid and 3D random fibre orientations were prepared and deformed in confined flows by performing continuous tests with a compression rheometer that was installed on a synchrotron X-ray microtomograph. The image acquisition parameters enabled the acquisition of 3D images with high spatial resolution and short scanning time (i.e., less than 0.5 s). An image analysis procedure was specifically developed and enabled the extraction of several key microstructure descriptors such as the positions and orientations of fibres and their contacts. The evolution of these descriptors was followed using a semi-discrete correlation technique of the spatial positions of fibre centrelines [74].

These experiments enabled the 3D observation and characterisation of a confined plane strain compression test of a concentrated fibre suspension. The quantitative analysis of the 3D images led to original results that clearly emphasised the complex kinematics of individual fibres. Large fluctuations in the translational and rotational fields of the fibres were observed during plane strain compression. These fluctuations were shown to be on the same order of magnitude than the mean fields. The kinematics of fibres was found to be different from that observed for dilute and semi-dilute fibre suspensions under similar confined flow conditions [48,49]. We also observed that contacts between fibres induce locally very strong perturbations in the fibre motion, leading to fibres kinematics that are far from the affine field and local Jeffery's equation predictions. This emphasises the central role played by the interactions between fibres on the rheology of these concentrated suspensions.

Surprisingly, in spite of the chaotic kinematics of the fibres, the macroscopic deformation of the suspension was quasi homogeneous and the overall fibre orientation in the suspension was found to be well described by the second order orientation tensor estimated from the integration of Jeffery's equation for each fibre of the suspension during compression. In addition, our results showed that the statistical tube model [65] was relevant to estimate the mean number of fibre-fibre contacts per fibre in concentrated fibre systems. The knowledge of the number of contacts is crucial to feed rheological models that enable estimating the predominant contribution of contacts to the overall stress field [7,29,72] within such systems.

The experimental results obtained in this study are promising and would enable improving micromechanical models and upscaling approaches related to the rheology modelling of concentrated fibre suspensions [7]. This approach would also enable an in-depth characterisation of the fibre mesostructures (fibre aggregates) present in these suspensions (Fig. 8). This would help understanding the complex micromechanics of these mesostructures and would help revealing the role they play on the rheology of concentrated fibre suspensions.

Declaration of Competing Interest

The authors declare that they have no known competing financial interests or personal relationships that could have appeared to influence the work reported in this paper.

Data availability

Data will be made available on request.

Acknowledgments

This research was supported by IDEX Université Grenoble Alpes and LabEx Tec21. The authors gratefully acknowledge LabEX Tec 21 and the research site of INSA Lyon at Oyonnax for administrative and technical support. The laboratories 3SR is part of the LabEx Tec 21 (Investissements d'Avenir-grant agreement n°ANR-11-LABX-0030) and the Carnot Institute Polynat (n° ANR16-CARN-0025). We acknowledge the Paul Scherrer Institute, Villigen, Switzerland for provision of synchrotron radiation beamtime at beamline TOMCAT of the SLS and would like to thank A. Bonnin for assistance.

References

[1] L. Orgéas, P.J.J. Dumont, Sheet molding compounds. Wiley Encyclopedia of Composites, John Wiley & Sons, Ltd, 2012, pp. 1–36, https://doi.org/10.1002/9781118097298.weoc222.

[2] J. Férec, P. Laure, L. Silva, M. Vincent, 20 - Short fiber composite reinforcements, in: P. Boisse (Ed.), Composite Reinforcements for Optimum Performance (Second Edition), Woodhead Publishing, 2021, pp. 627–669, https://doi.org/10.1016/B978-0-12-819005-0.00020-4.

[3] S.G. Advani, K.-.T. Hsiao, Manufacturing Techniques For Polymer Matrix Composites (PMCs), Elsevier, 2012.

[4] D. Ferré-Sentis, P.J.J. Dumont, L. Orgéas, F. Martoïa, M. Sager, Rheological response of compressible SMCs under various deformation kinematics: experimental aspects and simple modelling approach, Compos. Part A: Appl. Sci. Manuf. 154 (2022), 106774, https://doi.org/10.1016/j.compositesa.2021.106774.

[5] S. Le Corre, P. Dumont, L. Orgéas, D. Favier, Rheology of highly concentrated planar fiber suspensions, J. Rheol. (N Y N Y) 49 (2005) 1029–1058, https://doi.org/10.1122/1.1993594.

[6] O. Guiraud, L. Orgéas, P.J.J. Dumont, S. Rolland du Roscoat, Microstructure and deformation micromechanisms of concentrated fiber bundle suspensions: an analysis combining x-ray microtomography and pull-out tests, J. Rheol. (N Y N Y) 56 (2012) 593–623, https://doi.org/10.1122/1.3698185.

[7] L. Orgéas, P. Dumont, S.L. Corre, 5 - Rheology of highly concentrated fiber suspensions, in: F. Chinesta, G. Ausias (Eds.), Rheology of Non-Spherical Particle Suspensions, Elsevier, 2015, pp. 119–166, https://doi.org/10.1016/B978-1-78548-036-2.50005-8.

[8] J. Férec, E. Bertevas, G. Ausias, N. Phan-Thien, 4 - Macroscopic modeling of the evolution of fiber orientation during flow, in: T.D. Papathanasiou, A. Bénard (Eds.), Flow-Induced Alignment in Composite Materials (Second Edition), Woodhead Publishing, 2022, pp. 77–121, https://doi.org/10.1016/B978-0-12-818574-2.00002-6.

[9] G.B. Jeffery, L.N.G. Filon, The motion of ellipsoidal particles immersed in a viscous fluid, Proc. R. Soc. London. Series A 102 (1922) 161–179, https://doi.org/10.1098/rspa.1922.0078. Containing Papers of a Mathematical and Physical Character.

[10] H. Brenner, Rheology of a dilute suspension of axisymmetric Brownian particles, Int. J. Multiphase Flow 1 (1974) 195–341, https://doi.org/10.1016/0301-9322(74)90018-4.

[11] G.I. Taylor, The motion of ellipsoidal particles in a viscous fluid, Proc. R. Soc. London. Series A 103 (1923) 58–61, https://doi.org/10.1098/rspa.1923.0040. Containing Papers of a Mathematical and Physical Character.

[12] R.C. Binder, The motion of cylindrical particles in viscous flow, J. Appl. Phys. 10 (1939) 711–713, https://doi.org/10.1063/1.1707254.

[13] B.J. Trevelyan, S.G. Mason, Particle motions in sheared suspensions. I. Rotations, J. Colloid Sci. 6 (1951) 354–367, https://doi.org/10.1016/0095-8522(51)90005-0.

[14] M.P. Petrich, D.L. Koch, C. Cohen, An experimental determination of the stress–microstructure relationship in semi-concentrated fiber suspensions, J. Nonnewton. Fluid Mech. 95 (2000) 101–133, https://doi.org/10.1016/S0377-0257(00)00172-5.

[15] F.P. Bretherton, The motion of rigid particles in a shear flow at low Reynolds number, J. Fluid Mech. 14 (1962) 284–304, https://doi.org/10.1017/S002211206200124X.

[16] S.G. Advani, C.L. Tucker, The use of tensors to describe and predict fiber orientation in short fiber composites, J. Rheol. (N Y N Y) 31 (1987) 751–784, https://doi.org/10.1122/1.549945.

[17] E. Anczurowski, S.G. Mason, Particle motions in sheared suspensions. XXIV. Rotation of rigid spheroids and cylinders, Trans. Soc. Rheol. 12 (1968) 209–215, https://doi.org/10.1122/1.549106.

[18] M. Rahnama, D.L. Koch, C. Cohen, Observations of fiber orientation in suspensions subjected to planar extensional flows, Phys. Fluids 7 (1995) 1811–1817, https://doi.org/10.1063/1.868758.

[19] S. Sinha-Ray, K. Fezzaa, A.L. Yarin, The internal structure of suspensions in uniaxial elongation, J. Appl. Phys. 113 (2013), 044906, https://doi.org/10.1063/1.4789819.

[20] E.S.G. Shaqfeh, D.L. Koch, The effect of hydrodynamic interactions on the orientation of axisymmetric particles flowing through a fixed bed of spheres or fibers, Phys. Fluids. 31 (1988) 728–743. https://doi.org/10.1063/1.866809.

[21] C.A. Stover, D.L. Koch, C. Cohen, Observations of fibre orientation in simple shear flow of semi-dilute suspensions, J. Fluid Mech. 238 (1992) 277–296, https://doi.org/10.1017/S002211209200171X.

[22] E.S.G. Shaqfeh, D.L. Koch, Orientational dispersion of fibers in extensional flows, Phys. Fluids A: Fluid Dyn. 2 (1990) 1077–1093, https://doi.org/10.1063/1.857608.

[23] M. Rahnama, D.L. Koch, Y. Iso, C. Cohen, Hydrodynamic, translational diffusion in fiber suspensions subject to simple shear flow, Phys. Fluids A: Fluid Dyn. 5 (1993) 849–862, https://doi.org/10.1063/1.858890.

[24] G.H. Fredrickson, E.S.G. Shaqfeh, Heat and mass transport in composites of aligned slender fibers, Phys. Fluids A: Fluid Dyn. 1 (1989) 3–20, https://doi.org/10.1063/1.857546.

[25] E.S.G. Shaqfeh, G.H. Fredrickson, The hydrodynamic stress in a suspension of rods, Phys. Fluids A: Fluid Dyn. 2 (1990) 7–24, https://doi.org/10.1063/1.857683.

[26] P. Dumont, J.-.P. Vassal, L. Orgéas, V. Michaud, D. Favier, J.-A.E. Månson, Processing, characterisation and rheology of transparent concentrated fibre-bundle suspensions, Rheol. Acta 46 (2007) 639–651, https://doi.org/10.1007/s00397-006-0153-8.

[27] T.-.H. Le, P.J.J. Dumont, L. Orgéas, D. Favier, L. Salvo, E. Boller, X-ray phase contrast microtomography for the analysis of the fibrous microstructure of SMC composites, Compos. Part A: Appl. Sci. Manuf. 39 (2008) 91–103, https://doi.org/10.1016/j.compositesa.2007.08.027.

[28] P.J.J. Dumont, S. Le Corre, L. Orgéas, D. Favier, A numerical analysis of the evolution of bundle orientation in concentrated fibre-bundle suspensions, J. Nonnewton. Fluid Mech. 160 (2009) 76–92, https://doi.org/10.1016/j.jnnfm.2009.03.001.

[29] J. Férec, G. Ausias, 4 - Rheological modeling of non-dilute rod suspensions, in: F. Chinesta, G. Ausias (Eds.), Rheology of Non-Spherical Particle Suspensions, Elsevier, 2015, pp. 77–117, https://doi.org/10.1016/B978-1-78548-036-2.50004-6.

[30] F. Folgar, C.L. Tucker, Orientation behavior of fibers in concentrated suspensions, J. Reinf. Plast. Compos. 3 (1984) 98–119, https://doi.org/10.1177/073168448400300201.

[31] C.-.C. Lee, F. Folgar, C.L. Tucker, Simulation of compression molding for fiber-reinforced thermosetting polymers, J. Eng. Ind. 106 (1984) 114–125, https://doi.org/10.1115/1.3185921.

[32] R.S. Bay, Fiber Orientation in Injection-Molded Composites: a Comparison of Theory and Experiment, University of Illinois at Urbana-Champaign, 1991.

[33] N. Phan-Thien, X.-.J. Fan, R.I. Tanner, R. Zheng, Folgar–Tucker constant for a fibre suspension in a Newtonian fluid, J. Nonnewton. Fluid Mech. 103 (2002) 251–260.

[34] D.L. Koch, A model for orientational diffusion in fiber suspensions, Phys. Fluids 7 (1995) 2086–2088, https://doi.org/10.1063/1.868455.

[35] X. Fan, N. Phan-Thien, R. Zheng, A direct simulation of fibre suspensions, J. Nonnewton. Fluid Mech. 74 (1998) 113–135, https://doi.org/10.1016/S0377-0257(97)00050-5.

[36] J.H. Phelps, C.L. Tucker, An anisotropic rotary diffusion model for fiber orientation in short- and long-fiber thermoplastics, J. Nonnewton. Fluid Mech. 156 (2009) 165–176, https://doi.org/10.1016/j.jnnfm.2008.08.002.

[37] G.L. Hand, A theory of anisotropic fluids, J. Fluid Mech. 13 (1962) 33–46, https://doi.org/10.1017/S0022112062000476.

[38] G.G. Lipscomb, M.M. Denn, D.U. Hur, D.V. Boger, The flow of fiber suspensions in complex geometries, J. Nonnewton. Fluid Mech. 26 (1988) 297–325, https://doi.org/10.1016/0377-0257(88)80023-5.

[39] J.S. Cintra, C.L. Tucker, Orthotropic closure approximations for flow-induced fiber orientation, J. Rheol. (N Y N Y) 39 (1995) 1095–1122, https://doi.org/10.1122/1.550630.

[40] F. Dupret, A. Couniot, O. Mal, L. Vanderschuren, O. Verhoyen, Modelling and simulation of injection molding, in: D.A. Siginer, D. De Kee, R.P. Chhabra (Eds.), Modelling and simulation of injection molding, Rheology Series (1999) 939–1010, https://doi.org/10.1016/S0169-3107(99)80012-4.

[41] D.H. Chung, T.H. Kwon, Invariant-based optimal fitting closure approximation for the numerical prediction of flow-induced fiber orientation, J. Rheol. (N Y N Y) 46 (2002) 169–194, https://doi.org/10.1122/1.1423312.

[42] R.L. Schiek, E.S.G. Shaqfeh, Oscillatory shear of a confined fiber suspension, J. Rheol. (N Y N Y) 41 (1997) 445–466, https://doi.org/10.1122/1.550808.

[43] B. Snook, E. Guazzelli, J.E. Butler, Vorticity alignment of rigid fibers in an oscillatory shear flow: role of confinement, Phys. Fluids 24 (2012), 121702, https://doi.org/10.1063/1.4770141.

[44] H. Diamant, Hydrodynamic interaction in confined geometries, J. Phys. Soc. Japan 78 (2009), 041002–041002.

[45] W.B. Russel, E.J. Hinch, L.G. Leal, G. Tieffenbruck, Rods falling near a vertical wall, J. Fluid Mech. 83 (1977) 273–287, https://doi.org/10.1017/S0022112077001190.

[46] K.B. Moses, S.G. Advani, A. Reinhardt, Investigation of fiber motion near solid boundaries in simple shear flow, Rheol. Acta. 40 (2001) 296–306, https://doi.org/10.1007/s003970000135.

[47] R. Holm, D. Söderberg, Shear influence on fibre orientation, Rheol. Acta 46 (2007) 721–729, https://doi.org/10.1007/s00397-007-0166-y.

[48] T. Laurencin, L. Orgéas, P.J.J. Dumont, S. Rolland du Roscoat, P. Laure, S. Le Corre, L. Silva, R. Mokso, M. Terrien, 3D real-time and in situ characterisation of fibre kinematics in dilute non-Newtonian fibre suspensions during confined and lubricated compression flow, Compos. Sci. Technol. 134 (2016) 258–266, https://doi.org/10.1016/j.compscitech.2016.09.004.

[49] T. Laurencin, P. Laure, L. Orgéas, P.J.J. Dumont, L. Silva, S. Rolland du Roscoat, Fibre kinematics in dilute non-Newtonian fibre suspensions during confined and lubricated squeeze flow: direct numerical simulation and analytical modelling, J. Nonnewton. Fluid Mech. 273 (2019), 104187, https://doi.org/10.1016/j.jnnfm.2019.104187.

[50] C.A. Stover, C. Cohen, The motion of rodlike particles in the pressure-driven flow between two flat plates, Rheol. Acta 29 (1990) 192–203, https://doi.org/10.1007/BF01331355.

[51] A. Ozolins, U. Strautins, Simple models for wall effect in fiber suspension flows, Math. Modell. Anal. 19 (2014) 75–84, https://doi.org/10.3846/13926292.2014.893263.

[52] M. Perez, A. Scheuer, E. Abisset-Chavanne, F. Chinesta, R. Keunings, A multi-scale description of orientation in simple shear flows of confined rod suspensions, J. Nonnewton. Fluid Mech. 233 (2016) 61–74, https://doi.org/10.1016/j.jnnfm.2016.01.011.

[53] E. Bartram, H.L. Goldsmith, S.G. Mason, Particle motions in non-Newtonian media, Rheol. Acta 14 (1975) 776–782, https://doi.org/10.1007/BF01521406.

[54] Y. Iso, D.L. Koch, C. Cohen, Orientation in simple shear flow of semi-dilute fiber suspensions 1. Weakly elastic fluids, J. Nonnewton. Fluid Mech. 62 (1996) 115–134, https://doi.org/10.1016/0377-0257(95)01404-7.

[55] Y. Iso, C. Cohen, D.L. Koch, Orientation in simple shear flow of semi-dilute fiber suspensions 2. Highly elastic fluids, J. Nonnewton. Fluid Mech. 62 (1996) 135–153, https://doi.org/10.1016/0377-0257(95)01405-5.
[56] S.J. Johnson, A.J. Salem, G.G. Fuller, Dynamics of colloidal particles in sheared, non-Newtonian fluids, J. Nonnewton. Fluid Mech. 34 (1990) 89–121, https://doi.org/10.1016/0377-0257(90)80013-P.
[57] D.Z. Gunes, R. Scirocco, J. Mewis, J. Vermant, Flow-induced orientation of non-spherical particles: effect of aspect ratio and medium rheology, J. Nonnewton. Fluid Mech. 155 (2008) 39–50, https://doi.org/10.1016/j.jnnfm.2008.05.003.
[58] J. Férec, E. Bertevas, B.C. Khoo, G. Ausias, N. Phan-Thien, Rigid fiber motion in slightly non-Newtonian viscoelastic fluids, Phys. Fluids 33 (2021), 103320.
[59] G. D'Avino, P.L. Maffettone, Particle dynamics in viscoelastic liquids, J. Nonnewton. Fluid Mech. 215 (2015) 80–104, https://doi.org/10.1016/j.jnnfm.2014.09.014.
[60] P. Brunn, The slow motion of a rigid particle in a second-order fluid, J. Fluid Mech. 82 (1977) 529–547, https://doi.org/10.1017/S0022112077000822.
[61] D. Borzacchiello, E. Abisset-Chavanne, F. Chinesta, R. Keunings, Orientation kinematics of short fibres in a second-order viscoelastic fluid, Rheol. Acta 55 (2016) 397–409, https://doi.org/10.1007/s00397-016-0929-4.
[62] K. Yasuda, N. Mori, K. Nakamura, A new visualization technique for short fibers in a slit flow of fiber suspensions, Int. J. Eng. Sci. 40 (2002) 1037–1052, https://doi.org/10.1016/S0020-7225(01)00107-0.
[63] K. Yasuda, T. Kyuto, N. Mori, An experimental study of flow-induced fiber orientation and concentration distributions in a concentrated suspension flow through a slit channel containing a cylinder, Rheol. Acta 43 (2004) 137–145, https://doi.org/10.1007/s00397-003-0328-5.
[64] H. Menendez, J.L. White, A Wide-angle X-ray diffraction method of determining chopped fiber orientation in composites with application to extrusion through dies, Polym. Eng. Sci. 24 (1984) 1051–1055, https://doi.org/10.1002/pen.760241310.
[65] S. Toll, Note: on the tube model for fiber suspensions, J. Rheol. (N Y N Y) 37 (1993) 123–125, https://doi.org/10.1122/1.550460.
[66] L. Orgéas, P.J.J. Dumont, J.-.P. Vassal, O. Guiraud, V. Michaud, D. Favier, In-plane conduction of polymer composite plates reinforced with architectured networks of Copper fibres, J. Mater. Sci. 47 (2012) 2932–2942, https://doi.org/10.1007/s10853-011-6126-z.
[67] P. Latil, L. Orgéas, C. Geindreau, P.J.J. Dumont, S. Rolland du Roscoat, Towards the 3D in situ characterisation of deformation micro-mechanisms within a compressed bundle of fibres, Compos. Sci. Technol. 71 (2011) 480–488, https://doi.org/10.1016/j.compscitech.2010.12.023.
[68] D. Paganin, S.C. Mayo, T.E. Gureyev, P.R. Miller, S.W. Wilkins, Simultaneous phase and amplitude extraction from a single defocused image of a homogeneous object, J. Microsc. 206 (2002) 33–40, https://doi.org/10.1046/j.1365-2818.2002.01010.x.
[69] M.A. Beltran, D.M. Paganin, K. Uesugi, M.J. Kitchen, 2D and 3D X-ray phase retrieval of multi-material objects using a single defocus distance, Opt. Express, OE. 18 (2010) 6423–6436, https://doi.org/10.1364/OE.18.006423.
[70] C. Pudney, Distance-ordered homotopic thinning: a skeletonization algorithm for 3D digital images, Comput. Vis. Image Underst. 72 (1998) 404–413, https://doi.org/10.1006/cviu.1998.0680.
[71] C. Balbinot, F. Martoïa, P.J.J. Dumont, L. Orgéas, J.-.F. Bloch, S. Rolland du Roscoat, E. Boller, F. Flin, P. Carion, P. Latil, In situ 3D observations of capillary-driven flows in parallel arrangements of rigid fibres using X-ray microtomography, Compos. Part A: Appl. Sci. Manuf. 157 (2022), 106941, https://doi.org/10.1016/j.compositesa.2022.106941.
[72] M. Djalili-Moghaddam, S. Toll, A model for short-range interactions in fibre suspensions, J. Nonnewton. Fluid Mech. 132 (2005) 73–83, https://doi.org/10.1016/j.jnnfm.2005.08.014.
[73] J. Férec, G. Ausias, M.C. Heuzey, P.J. Carreau, Modeling fiber interactions in semiconcentrated fiber suspensions, J. Rheol. (N Y N Y) 53 (2009) 49–72, https://doi.org/10.1122/1.3000732.
[74] S. Le Corre, P. Latil, L. Orgéas, P.J.J. Dumont, S.R. du Roscoat, C. Geindreau, A 3D image analysis method for fibrous microstructures: discretization and fibers tracking, in: ECCM15 - 15th European Conference On Composite Materials, Venice, 2012.
[75] F. Martoïa, P.J.J. Dumont, L. Orgéas, M.N. Belgacem, J.-.L. Putaux, Micro-mechanics of electrostatically stabilized suspensions of cellulose nanofibrils under steady state shear flow, Soft Matter. 12 (2016) 1721–1735, https://doi.org/10.1039/C5SM02310F.
[76] L. Orgéas, P.J.J. Dumont, F. Martoïa, C. Marulier, S. Le Corre, D. Caillerie, On the role of fibre bonds on the elasticity of low-density papers: a micro-mechanical approach, Cellulose 28 (2021) 9919–9941, https://doi.org/10.1007/s10570-021-04098-w.